Catalysis Today 175 (2011) 124–132

Contents lists available at ScienceDirect

Catalysis Today

journal homepage: www.elsevier.com/locate/cattod

# Effect of barium loading on $CuO_x$–$CeO_2$ catalysts: $NO_x$ storage capacity, NO oxidation ability and soot oxidation activity

Fan Lin, Xiaodong Wu*, Duan Weng

*Laboratory of Advanced Materials, Department of Materials Science and Engineering, Tsinghua University, Beijing 100084, China*

ARTICLE INFO

*Article history:*
Received 12 October 2010
Received in revised form 1 February 2011
Accepted 1 March 2011
Available online 29 March 2011

*Keywords:*
Cu–Ce mixed oxides
Barium loading
Soot oxidation
NO oxidation
$NO_x$ storage

ABSTRACT

A series of Ba–Cu–Ce catalysts were prepared by loading different amounts of $Ba(Ac)_2$ on the sol–gel-synthesized $CuO_x$–$CeO_2$ mixed oxides. The activities of the catalysts for soot oxidation were evaluated in 1000 ppm NO/10% $O_2$/$N_2$ under loose contact conditions. The catalysts were characterized by XRD, BET, H2-TPR, in situ-DRIFTS and NO-TPO measurements. When Ba loading is between 6 and 10 mol.% of Cu + Ce, the catalysts exhibit an onset temperature ($T_i$) as low as 376 °C. NO is oxidized at $Cu^{x+}$ and $Ce^{x+}$ sites and then stored on the adjacent Ba species in form of barium nitrate. $Ba(NO_3)_3$ begins to decompose, releasing abundant $NO_2$ at around 370 °C under the driving of soot as the reductant. The nitrate-derived $NO_2$ and the NO-derived $NO_2$ initiate the soot combustion over the Ba-modified catalysts with a significantly lowered $T_i$. The ternary catalysts lose their $NO_x$ storage capacity after hydrothermally aged at 800 °C for 10 h due to the formation of $BaCeO_3$. However, Ba restrains the sintering of $(Cu,Ce)O_x$, resulting in relatively more favorable redox properties and thus higher activity for NO oxidation. The barium-modified catalysts show lower onset temperatures (470–480 °C) of soot oxidation than pure CuCe (509 °C) after aging.



## 1. Introduction

Diesel engines have gained favor in recent years due to their higher efficiency compared to gasoline engines. Particulate matter (PM), which is composed of aggregated carbonaceous soot and adsorbed hydrocarbon is often carcinogenic and is one of the main pollutants in diesel engine emissions [1] thus inciting researchers to control their emissions. The diesel particulate filter (DPF), when combined with soot catalytic combustion technology is the most efficient method to reduce the soot emission [2].

A lot of catalysts have been developed to reduce soot combustion temperature. Among them the noble metal catalysts are one of the most active kinds, as platinum can effectively catalyze NO oxidized to $NO_2$, which is a more powerful oxidant than $O_2$ [2,3]. However, the high cost of noble metals restricts its application. To reduce the cost of catalysts, cerium oxides [4–6], transition metal oxides [7,8] and their mixed oxides [9–13] as well as perovskite-type complex oxides [14,15] are being developed for catalyzing the soot oxidation. Nevertheless, the activities of mixed oxides catalysts are limited as they fail to reduce the $T_m$ (the maximum soot oxidation rate temperature) below 400 °C which is the normal upper limit for the temperature of diesel exhaust gas. To enhance the activity of catalysts, alkali metals mostly potassium have been introduced to the catalysis system [16–19]. The addition of potassium can reduce the $T_m$ to 350 °C or even lower. It is well known that the function of potassium is mainly based on the following factors: (i) the low molten point and mobility of potassium salts increase greatly the contact between soot and catalyst; and (ii) potassium, as a strong alkaline site, can store $NO_x$ in nitrate and nitrite form on the catalyst that decompose and release $NO_x$ at higher temperature to assist soot oxidation [16]. Despite the high activity, however, a drawback of K-containing catalysts emerges because of the low stability which comes along with the low melting point and solubility of the K species, especially in the presence of water [20].

Alkali earth metals such as barium also exhibit high a capacity for storing $NO_x$, thus they are widely studied in NSR ($NO_x$ storage reduction) catalysts for $NO_x$ reduction [21–24]. Since the presence of $NO_x$ can promote soot oxidation, the $NO_x$ storage features make barium a promising component in $NO_x$-assisted soot combustion catalyst However, most of the reported work has been concentrated on potassium-containing catalysts (such as Ba–K–Ce [25,26] and Co–Ba–K(Zr) [27,28]) and noble metal catalysts (such as Pt–Ba–Al [29,30]), whose drawbacks have been outlined above. Our group recently reported the promotional effect that barium has on the soot oxidation activity of $MnO_x$–$CeO_2$ [31] and $CoO_x$–$CeO_2$ mixed oxides [32] in the presence of NO.

Copper-based catalysts have been studied for soot oxidation due to the superior redox property of copper oxides [7,13]. In our previous work, $CuO_x$–$CeO_2$ mixed oxides were found to exhibit high activities for soot oxidation [33], and modifier components such

* Corresponding author. Tel.: +86 10 62792375; fax: +86 10 62792375.
*E-mail address:* wuxiaodong@tsinghua.edu.cn (X. Wu).

0920-5861/$ – see front matter © 2011 Elsevier B.V. All rights reserved.
doi:10.1016/j.cattod.2011.03.002

as potassium [19] and alumina [34] were added to improve the activity and stability of the catalyst. In this study, Ba was supported on Cu–Ce mixed oxides in order to enhance the $NO_x$ storage capacity of the catalyst and hereby promote the soot oxidation in the presence of $NO_x$. XRD, Raman, BET, $H_2$-TPR, in situ DRIFT and NO-TPO were conducted to characterize the structural, redox and adsorption/desorption properties of the catalysts. Finally, a possible mechanism of the $NO_x$-assisted soot oxidation with BaCuCe catalysts was explored.

## 2. Experimental

### 2.1. Catalyst preparation

$CuO_x$–$CeO_2$ mixed oxides were prepared through a citric sol–gel method. The nitrate precursors $Ce(NO_3)_3{\cdot}6H_2O$ (99.0 wt.%, Beijing Yili) and $Cu(NO_3)_2{\cdot}3H_2O$ (99.0 wt.%, Beijing Yili) were mixed in deionized water according to a molar ratio of Cu:Ce = 1:9. The citric acid was added to the solution as the complexing agent with the molar amount as twice that of total metal ions including $Ce^{3+}$ and $Cu^{2+}$. Polyglycol was also added as surface activating agent at a weight 10% that of the citric acid. The mixed solution was stirred vigorously with a magnetic stirrer and heated to 80 °C to vaporize the water until a gel was formed. The resulting gel was dried at 110 °C overnight followed by calcination at 300 °C for 1 h to decompose the organic species and at 500 °C for 3 h to for Cu–Ce mixed oxides. $CeO_2$ was prepared through a similar method.

Ba was loaded on the Cu–Ce mixed oxides by wetness impregnation method. $Ba(Ac)_2$ (99.0 wt.%, Shantou Xilong) solutions were incipiently taken by the pores of the Cu–Ce support. The loading amount of Ba was calculated according to the molar ratio of Ba:(Cu + Ce) = 0.03, 0.06, 0.1 and 0.15, respectively. The resulting mixture was dried at 110 °C for 2 h to remove water and was calcined at 550 °C for 1 h. The powders were cooled to room temperature in the furnace to obtain the Ba–Cu–Ce catalysts, referred to as BaCuCe3, BaCuCe6, BaCuCe10 and BaCuCe15, respectively. Ba was also loaded on $CeO_2$ in a molar ratio of Ba:Ce = 0.1 as a reference catalyst (denoted as BaCe10).

To obtain the hydrothermally aged samples, the as-prepared samples were placed in a tubular quartz reactor and treated under 10 vol% $H_2O$ at 800 °C for 10 h with a flow containing with a flow rate of 200 ml/min.

### 2.2. Catalyst characterization

The powder X-ray diffraction (XRD) experiments were determined with a Japan Science D/max-RB diffractometer employing Cu Kα radiation (λ = 1.5418 Å). The X-ray tube was operated at 40 kV and 120 mA. The X-ray powder diffractograms were recorded at 0.02° intervals in the range of $20° \leq 2\theta \leq 80°$ with a scanning velocity of 6°/min. The lattice constants and mean crystallite sizes of ceria in the samples were calculated from Cohen's method and the Williamson–Hall equation, respectively.

The Raman spectra were obtained with a LabRAM HR 800 (HORIBA Jobin Yvon, France) spectrometer under room temperature and atmospheric pressure. An argon ion laser beam with a wave length of 633 nm was focused on a spot of 1 μm in diameter.

The specific surface areas of the samples were measured using the $N_2$ adsorption isotherm at −196 °C with the four-point Brunauer–Emmett–Teller (BET) method through an automatic surface analyzer (Quantachrome NOVA 4000). The samples were degassed at 200 °C for 2 h prior to the test.

The $H_2$ temperature-programmed reduction ($H_2$-TPR) tests were performed in a fixed-bed reactor with the effluent gases monitored by a mass spectrometer (OmniStar TM). 25 mg of sample were sandwiched by quartz wool and placed in a tubular quartz reactor (i.d. = 10 mm). The reactor temperature was raised up to 900 °C at a heating rate of 10 °C/min in $H_2$ (5 vol%)/He (50 ml/min).

The NO temperature-programmed oxidation (TPO) tests were carried out in a fixed-bed reactor with the effluent gases monitored by an infrared spectrometer (Thermo Nicolet 380). The gas mixture of 1000 ppm NO/10% $O_2$/$N_2$ was fed to 100 mg of sample powders at a flow rate of 500 ml/min. The reactor temperature was ramped to 550 °C at a heating rate of 10 °C/min.

The diffuse reflectance infrared Fourier transformed (DRIFT) spectra were recorded on a Nicolet 6700 spectrometer equipped with a temperature-controlled diffuse reflection chamber and a highly sensitive MCT detector. The sample powders were purged in situ under a $N_2$ stream flow at 100 ml/min with a temperature of 450 °C for 30 min, and were then cooled down to room temperature. The background spectrum was taken at each temperature. Afterwards, a gas mixture of 1000 ppm NO/10% $O_2$/$N_2$ was fed at a flow rate of 100 ml/min. All the spectra were determined by accumulating 100 scans at a resolution of 4 $cm^{-1}$ as a function of temperature at a heating rate of 10 °C/min.

### 2.3. Catalyst activity measurement

Printex-U (Degussa) was used as the model soot. Its particle size was 25 nm and the specific surface area was 100 $m^2$/g. The catalytic activities of the catalysts for soot oxidation were evaluated in a temperature-programmed oxidation (TPO) reaction apparatus. 10 mg of soot and 100 mg of powder catalyst were mixed carefully in a 1/10 weight ratio with a spatula for "loose contact" conditions. The catalyst-soot mixture was sandwiched between quartz wools and placed in a tubular quartz reactor (i.d. = 10 mm), and the oxidation test was carried out in the temperature range from room temperature to 550 °C at a heating rate of 20 °C/min. The inlet gas mixture was 1000 ppm NO/10% $O_2$/$N_2$ introduced at a flow rate of 1000 ml/min. The concentrations of $CO_2$, CO and NO in the outlet gas mixture were determined on-line by a five-component analyzer FGA4015 with an infrared sensor. The test was carried out under heat transfer limitation conditions, where the temperature at which the rate of $CO_2$ generation increased abruptly was referred to as the ignition temperature ($T_i$) of soot oxidation, which could be observed on the TPO curve of $CO_2$ as an inflection point before $CO_2$ concentration reached the maximum. $T_i$ generally reflected the intrinsic characteristics of the catalytic material and was hardly affected by reaction conditions. $T_m$ represented the maximal soot oxidation rate temperature. The total molar ratio of $CO_2/(CO_2 + CO)$ in the outlet gas during soot oxidation process was defined as the selectivity to $CO_2$ ($S_{CO_2}$).

## 3. Results

### 3.1. XRD, Raman and BET

The powder XRD patterns of the fresh and aged samples are shown in Fig. 1. All the fresh samples present the characteristic peaks attributed to ceria with a cubic fluorite structure, and no copper oxide phases are detected. The lattice constants of ceria in the fresh samples including BaCe are similar to each other (around 0.5412–0.5415 nm) as listed in Table 1, denying the possibility of the formation of $CuO_x$–$CeO_2$ solid solutions. Thus, it is plausible that copper oxide clusters, which cannot be detected by X-ray, are highly dispersed on strong contact with ceria crystallites. The typical peaks of the $BaCO_3$ phase are observed with the intensity increasing as a function of the Ba loading amount. The diffraction peaks of $CeO_2$ are significantly sharpened because of severe sin-

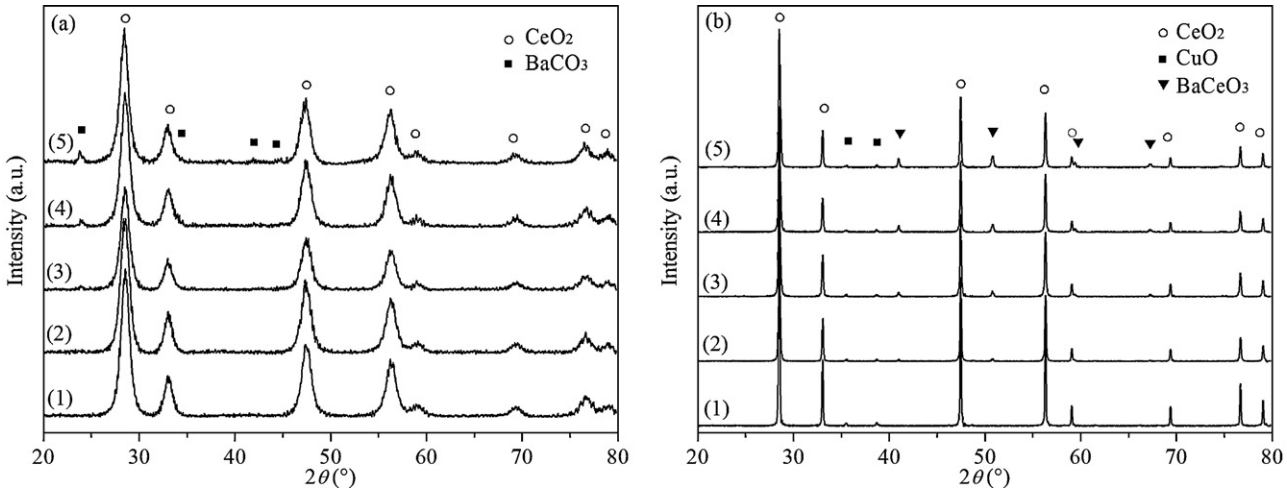


**Fig. 1.** XRD patterns of the (a) fresh and (b) hydrothermally aged catalysts: (1) CuCe, (2) BaCuCe3, (3) BaCuCe6, (4) BaCuCe10 and (5) BaCuCe15.

tering of ceria crystallites. The cubic CuO phase is also detected, indicating the segregation and growth of copper oxide crystallites. The peaks of $BaCeO_3$ perovskite-type oxide appear instead of $BaCO_3$ due to reaction between barium and cerium during the high-temperature calcination.

Table 1 shows that neither the addition of copper nor barium visibly affects the lattice constant of ceria. Although copper and cerium nitrates were mixed in the sol–gel process as precursors, the formation of $CuO_x$–$CeO_2$ solid solutions may be limited at the interfacial regions between copper oxide and ceria as reported by Chen et al. [35]. Table 1 also summarizes the mean crystallite sizes of $CeO_2$ and CuO and the BET surface areas of the samples. The loading of barium salts does not seem to affect the crystallite size of ceria (8.1–8.7 nm) in $CuO_x$–$CeO_2$ mixed oxides, while it does effectively inhibit the growth of ceria and copper oxide crystallites during aging. The surface area of the fresh sample decreases with the increase of the Ba loading due to blocking of the support pores by barium salts. The surface area of the catalysts and especially CuCe diminishes remarkably after aging.

The structural features of the catalysts are also described by Raman characterization. Fig. 2 shows the Raman spectra of two typical catalysts CuCe and BaCuCe10 with $CeO_2$ as reference. Pure $CeO_2$ presents a distinct band at 462 $cm^{-1}$, which is assigned to the cubic structure of $CeO_2$. This band shifts to 458 $cm^{-1}$ on CuCe-F and BaCuCe10-F, probably indicating a slight shrink of the ceria lattice due to formation of the $CuO_x$–$CeO_2$ solid solutions at the interfacial region which can hardly be detected by XRD. Shan et al. have reported a more obvious shift to 443 $cm^{-1}$ for $Ce_{0.9}Cu_{0.1}O_y$ solid solutions, which is ascribed to the changes in the lattice parameter resulting from the formation of the solid solutions [36]. The difference in band shift may be caused by the preparation methods applied and hereby the properties of the obtained mixed oxides

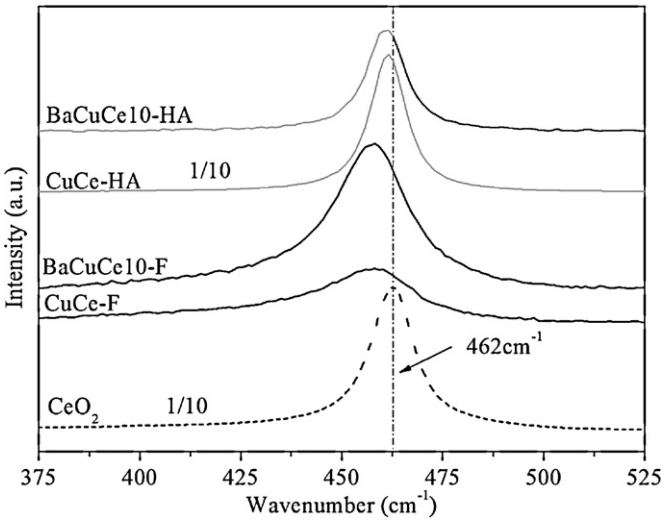


**Fig. 2.** Raman spectra of CuCe, BaCuCe10 and $CeO_2$.

such as the amount of oxygen vacancies and crystallite size of ceria [36,37]. Thus, it is suggested that the slight band shift on the home-made catalysts may be caused by the partial incorporation of copper ions into the ceria lattice at the interface region, which changes the $CeO_2$ environment with an increase of oxygen vacancies. For the aged samples CuCe-HA and BaCuCe10-HA, this band moves back towards 462 $cm^{-1}$ accompanied with the emergence of CuO band at 294.2 $cm^{-1}$ (not shown), indicating the segregation and sintering of $CeO_2$ and CuO.

**Table 1**
Structural properties of the catalysts.[a]

| Sample | Ba/(Cu + Ce) (molar ratio) | $a$[b] (nm) | $S_{BET}$ ($m^2$/g) | $d_{CeO_2}$[c] (nm) | $d_{CuO}$[c] (nm) |
|---|---|---|---|---|---|
| CuCe | – | 0.5412 (0.5415) | 72 (1.0) | 8.7 (97) | – (64) |
| BaCuCe3 | 0.03 | 0.5416 (0.5414) | 64 (2.8) | 8.1 (77) | – (46) |
| BaCuCe6 | 0.06 | 0.5415 (0.5415) | 60 (2.9) | 8.1 (54) | – (48) |
| BaCuCe10 | 0.10 | 0.5414 (0.5415) | 43 (3.0) | 8.6 (44) | – (55) |
| BaCuCe15 | 0.15 | 0.5414 (0.5415) | 34 (2.4) | 8.3 (39) | – (54) |
| BaCe | 0.10 | 0.5415 (0.5419) | 12 (4.1) | 13.1(27) | – |

[a] The values in parenthesis represent the corresponding data of the hydrothermally aged samples.
[b] Lattice constant of $CeO_2$ calculated by Cohen's method.
[c] Mean crystallite sizes of $CeO_2$ and CuO calculated according to Williamson–Hall equation.

**Table 2**
Activities of the catalysts for soot oxidation.[a]

| Sample[a] | $T_i$ (°C) | $T_m$ (°C) | $S_{CO_2}$ (%) |
|---|---|---|---|
| CuCe | 417 (509) | 433 (525) | 100 (98) |
| BaCuCe3 | 402 (477) | 416 (490) | 97 (99) |
| BaCuCe6 | 377 (469) | 395 (490) | 98 (98) |
| BaCuCe10 | 376 (469) | 400 (483) | 97 (99) |
| BaCuCe15 | 398 (474) | 414 (489) | 98 (97) |
| BaCe10 | 485 (512) | 508 (526) | 95 (89) |

[a] The values in parenthesis represent the corresponding data of the hydrothermally aged samples.

### 3.2. Soot-TPO

The activities of the catalysts were evaluated by the soot-TPO tests performed in an atmosphere of 1000 ppm NO/10% $O_2/N_2$ under loose contact conditions and a high flow rate of 1 l/min. The $T_i$ and $T_m$ of the fresh and hydrothermally aged samples are listed in Table 2. The fresh catalysts with the Ba loading content of 6–10% present the lowest $T_i$ values. After the hydrothermal aging treatment, the activity of the Ba-free CuCe catalyst deteriorates drastically with a shift of both $T_i$ and $T_m$ to higher temperatures by more than 90 °C. The aged Ba-containing catalysts remain relatively higher reactivity than the aged CuCe. For example, the aged BaCuCe10 exhibits the lowest $T_m$ at 483 °C, which is lower than that of the aged CuCe by 42 °C. The Ba-containing catalysts differ little in activity after aging due to severe sintering and diffusion of the oxides. The product of soot catalytic oxidation is almost completely $CO_2$ for all the catalysts, indicating a high efficiency of CO oxidation if it is produced. In the absence of the transition metal as strong oxidative component, the BaCe catalyst exhibits a much lower activity and selectivity.

In order to further explore $NO_x$ assistance for soot catalytic oxidation, the soot-TPO tests were carried out in gas flows with various NO concentrations from zero to 5000 ppm. The relationships between the $T_i$ and NO concentration on BaCuCe10-F and CuCe-F are shown in Fig. 3. In the absence of NO, BaCuCe10-F appears slightly delayed $T_i$ (522 °C) compared with CuCe-F (517 °C), indicating a slightly weakened redox ability by loading barium salt which will be confirmed by $H_2$-TPR curves in Section 3.3. It can be obviously seen that NO concentration influences soot catalytic oxidation in a different way for the catalysts with and without Ba. By introduction of a small concentration of NO (300 ppm) to the reaction atmosphere, the $T_i$ of BaCuCe10-F decreases much more sharply than that of CuCe-F. After the inlet NO concentration reaches 1000 ppm, the $T_i$ (376 °C) of BaCuCe10-F does not reduce any more with further increase of NO concentration. Meanwhile, the $T_i$ of CuCe-F keeps decreasing to ca. 350 °C when the concentration of NO is as high as 5500 ppm. Such different dependencies on

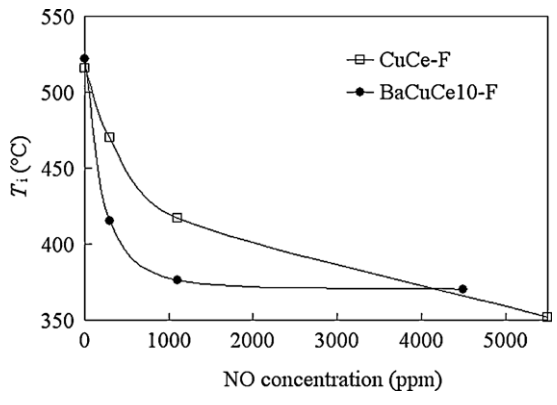


**Fig. 3.** Relationship between the $T_i$ for soot oxidation and the inlet NO concentration.

NO concentration may be related to the coverage of active sites by the stored nitrate/nitrite species for BaCuCe10-F. On the other hand, more NO is oxidized to $NO_2$ on CuCe-F as the NO concentration increases, resulting in an elevated soot catalytic oxidation activity. These results indicate a more obvious effect of $NO_x$ on soot oxidation on the Ba-containing catalyst at low NO level. With respect to the relatively low $NO_x$ emissions and low average exhaust gas temperatures of modern diesel engines, the BaCuCe catalyst exhibits a more promising way to remove soot additionally enhanced by desorption of $NO_2$ being stored at lower temperatures.

In order to observe the role of $NO_x$ in soot oxidation more clearly, the soot-TPO curves of the fresh and aged BaCuCe10, CuCe and BaCe catalysts are shown in Fig. 4a and b, respectively. For the fresh samples, a sharp rise of NO appears simultaneously with the onset of soot oxidation with BaCuCe10-F, which is not observed on the bimetal catalysts CuCe-F and BaCe-F at lower activities. For CuCe-F, the $CO_2$ production accelerates gradually from about 350 °C until extensive combustion occurs at about 420 °C. The uptake of NO during soot oxidation could be ascribed to the conversion of NO to $NO_2$ and limited reduction to $N_2$. BaCe-F exhibits a poor activity, and a flat NO line reflects the low redox ability and $NO_x$ storage capacity.

It has been widely reported that NO concentration has a significant influence on soot oxidation rate and that the $NO_x$-assistant function can be expressed through the following reactions [38]:

$$NO + O_2 \rightarrow NO_2 \quad (1)$$

$$NO_2 + C \rightarrow CO_2 + NO \quad (2)$$

The $NO_2$ produced by NO oxidation (Eq. (1)) acts as a powerful oxidant for soot oxidation at mild temperature (Eq. (2)). This is the case for CuCe catalyst where the reaction rate increases mildly with temperature until at 420 °C when the oxidation rate is fast enough to produce heat to promote the extensive burning of soot by $O_2$. The case is different for the BaCuCe10-F catalyst on which the soot burns at lower temperature (around 376 °C) accompanied with a sharp NO increase. It makes sense to suggest that the soot is ignited not only by the $NO_2$ derived from NO oxidation but also by that from the decomposition of nitrate stored at lower temperatures. A theorized mechanism will be given in Section 4.

This NO rise with the ignition of soot vanishes on the BaCuCe catalyst after aging as shown in Fig. 4b. The similar NO behaviors of the aged catalysts imply the same reaction mechanism although BaCuCe10-HA still exhibits some superior activity. As indicated by the XRD and BET results, the loss of $NO_x$ storage capacity of the aged BaCuCe catalysts is caused by the formation of $BaCeO_3$, the greatly reduced surface areas of catalysts and the seriously weakened synergistic effect between copper and ceria. It has been reported that the $NO_x$ storage capacity of bulk $BaCeO_3$ is much poorer than that of active $BaCO_3$ crystallites [39,40]. Nevertheless, it may be favorable that the formation of these perovskite-type oxides can be greatly restrained during the aging treatment in an atmosphere containing $CO_2$ which is a common component of exhaust gas from diesel engine [39–41]. The less diminished activity of BaCuCe10-HA is theoretically ascribed to the inhibition effect of barium on the sintering of ceria.

To verify the importance of the nitrate-derived $NO_2$ in soot oxidation, the catalysts were pretreated in a gas flow of 1000 ppm NO/10% $O_2/N_2$ at 350 °C for 30 min for $NO_x$ storage, followed by a soot-TPO test in 10% $O_2/N_2$. The evolutions of NO and $CO_2$ during the oxidation process are shown in Fig. 5. Although NO is absent in the inlet gas flow, BaCuCe10-F, pretreated in $NO/O_2$, reveals a high activity with the $T_i$ located at 375 °C which is comparable to that obtained in the presence of $NO + O_2$ (376 °C). Similarly, the onset of soot oxidation is also accompanied by a distinct peak of NO released. The maximal concentration of NO (about 7000 ppm) in this process is even higher than that in Fig. 4a, which may be

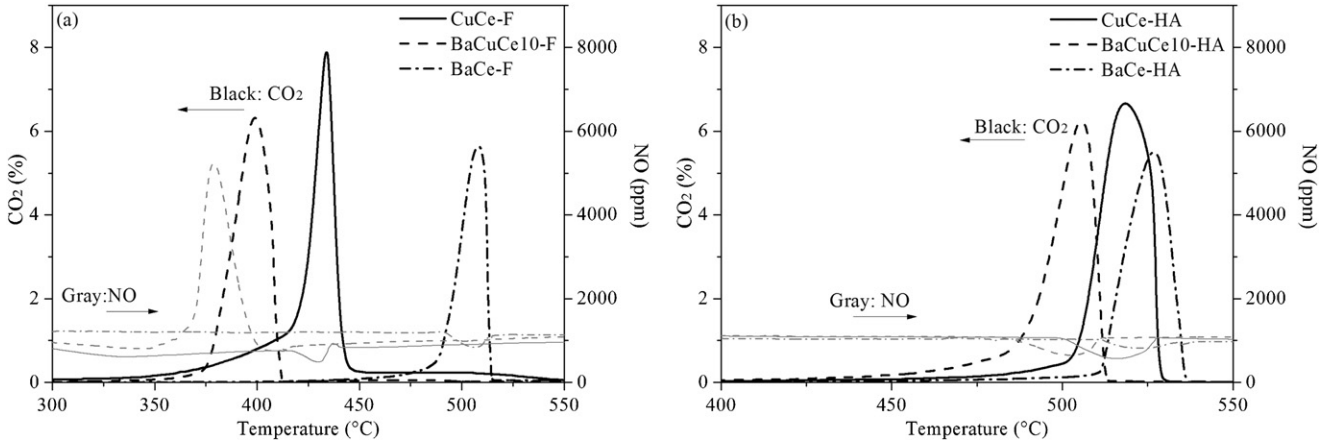


**Fig. 4.** Evolutions of $CO_2$ and NO during soot-TPO tests of the (a) fresh and (b) hydrothermally aged CuCe, BaCuCe10 and BaCe.

ascribed to more nitrates stored during pretreatment in $NO + O_2$. Contrarily, the $NO_x$ pretreatment does not result in any obvious NO desorption or decrease in the $T_i$ for CuCe-F. Only a little NO is released on BaCe-F at the temperatures lower than 420 °C, which contributes little to soot oxidation since it does not match the temperature interval of soot catalytic oxidation. According to the above results, it can be concluded that the nitrate-derived $NO_2$ is an important oxidant to initiate the soot oxidation at relatively low temperatures (<400 °C) and itself is reduced to NO.

### 3.3. $H_2$-TPR

The $H_2$-TPR tests were applied to evaluate the redox properties of the catalysts. The results are shown in Fig. 6. A bimodal shape of overlapped double peaks is observed between 140 and 210 °C for all the fresh samples, which are ascribed to the stepwise reduction of surface dispersed $CuO_x$ clusters, i.e. $Cu^{2+} \rightarrow Cu^{+}$ and $Cu^{+} \rightarrow Cu^{0}$ [42,43]. In addition, $H_2$ consumption of the peak at 210 °C is larger than that of the peak at 140 °C, which may be ascribed to the reduction of $Cu^{+}$ to $Cu^{0}$ occurring before the end of the former one due to the influence of $H_2$ spillover as reported elsewhere [42]. These peaks shift towards higher temperatures with an increase in Ba loading, indicating that the redox property of catalyst is weakened due to covering of catalyst surface by Ba salts. This result explains the delayed onset temperature of BaCuCe10-F with respect to CuCe-F in $O_2$. Minor peaks are observed in the temperature range from 350 to 500 °C, which always appear due to the reduction of surface oxygen species including hydroxyl groups. A broad peak in the temperature range of 700–900 °C is observed on CuCe-F, which is ascribed to the reduction of lattice oxygen from ceria [44]. The peak centered at 700 °C that increases proportionally with Ba amount is ascribed to the water-gas-shift (WGS) reaction of $CO_2$ from decomposition of $BaCO_3$ on $Ce^{x+}$ and $Cu^{x+}$ active sites, as CO is produced simultaneously with the consumption of $H_2$.

The XRD results show that the sintering of ceria can be inhibited to some extent by loading barium. Estimating the mean crystallite size of CuO in the aged samples is difficult due to the low intensities of the diffraction peaks of copper oxide. However, it can be indirectly confirmed by the $H_2$-TPR curves of the aged samples in Fig. 6b that a similar inhibition effect on sintering of copper oxide is attained by loading of barium. The bimodal shape of overlapped double peaks turns to be a single peak at 350 °C for CuCe-HA, which can be assigned to the reduction peak of crystalline CuO. Meanwhile, the reduction peaks of copper oxide on the aged Ba-containing samples are centered at around 310 °C, revealing a less severe clustering of copper oxides. The residual low-temperature peak (<250 °C) is observed on BaCuCe3-HA and BaCuCe6-HA, which is ascribed to the reduction of $CuO_x$ clusters in high dispersion state since the mean crystallite size of CuO in Table 1 has revealed a less sintering of CuO on these two aged catalysts.

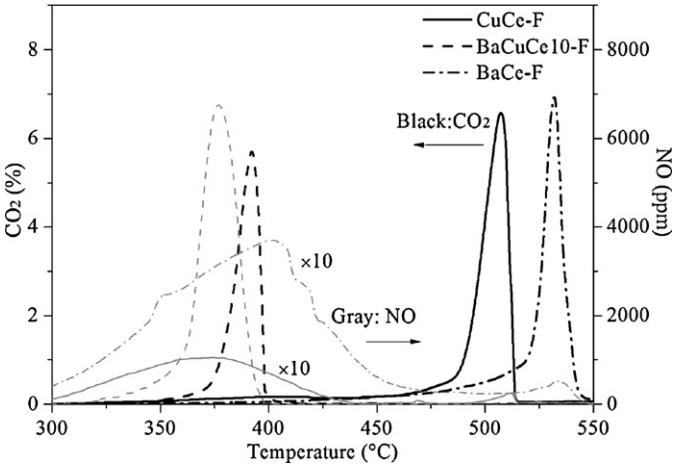


**Fig. 5.** Evolutions of NO and $CO_2$ during soot-TPO tests in 10% $O_2/N_2$ with the $NO_x$-pretreated catalysts.

### 3.4. NO-TPO

The conversion of NO to $NO_2$ is important for soot catalytic oxidation. Unfortunately, the apparatus applied for soot-TPO can only detect NO. To clarify the redox and absorption properties for $NO_x$ on the catalysts, NO-TPO as well as in situ DRIFTS were carried out in the absence of soot.

Fig. 7 shows the evolutions of the downstream NO, $NO_2$ and total $NO_x$ ($NO + NO_2$) during the NO-TPO tests on the typical CuCe and BaCuCe10 catalysts. NO can be effectively oxidized to $NO_2$ on BaCuCe10-F and CuCe-F. CuCe-F reveals a lower onset temperature of NO oxidation at 200 °C with respect to the Ba-containing catalyst (250 °C). On the other hand, the $NO_x$ adsorption capacity is completely different with these two catalysts. BaCuCe10-F shows a strong $NO_x$ absorption capacity with a distinct $NO_x$ uptake in the temperature range from 200 to 370 °C, while only a small $NO_x$ absorption is observed at around 200 °C on CuCe-F. The NO uptake below 100 °C followed by a NO release at 100–180 °C is ascribed to the weak adsorption of $NO_x$.

The NO oxidation activities and $NO_x$ adsorption capacity of both catalysts are severely diminished after aging. However, BaCuCe10-HA still shows a relatively high NO oxidation activity compared

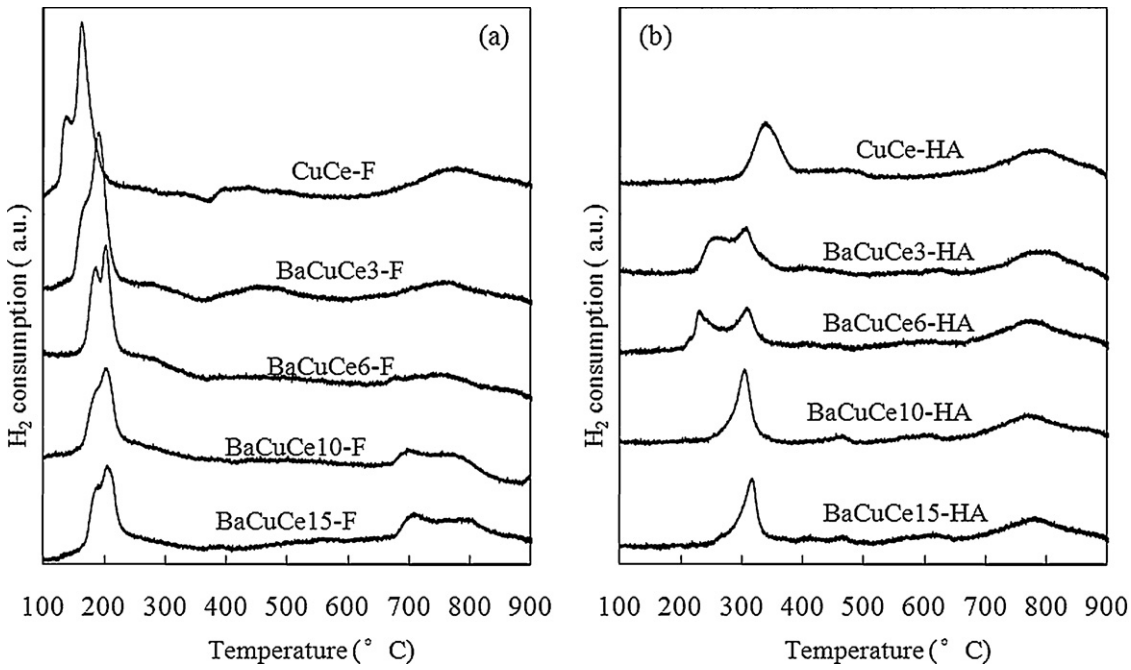


**Fig. 6.** $H_2$-TPR profiles of the (a) fresh and (b) hydrothermal aged catalysts.

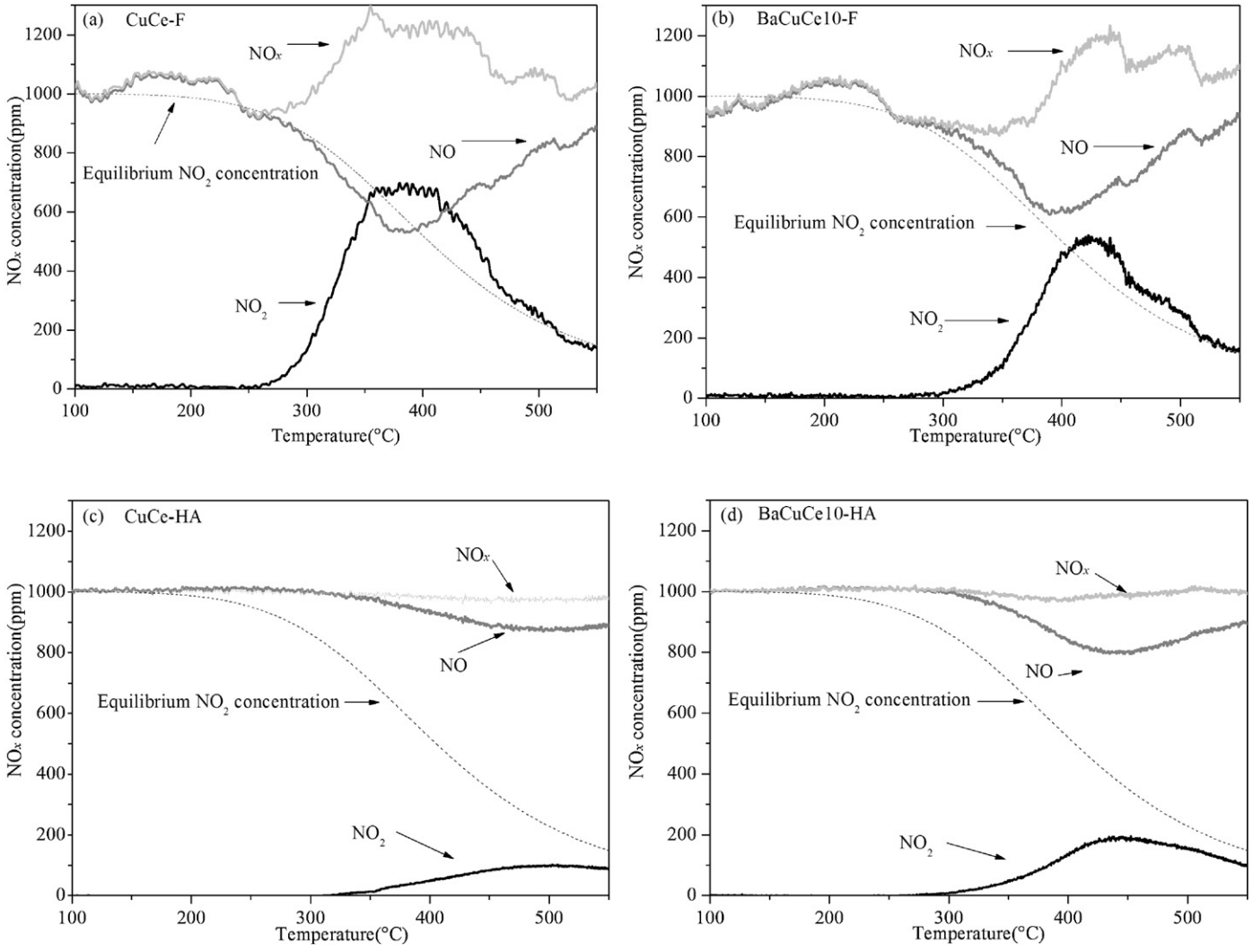


**Fig. 7.** NO-TPO profiles of (a) CuCe-F, (b) BaCuCe10-F, (c) CuCe-HA and (d) BaCuCe10-HA.

to CuCe-HA, which is in accordance with the $H_2$-TPR results and explains its higher soot oxidation activity. In this case, the NO-derived $NO_2$ rather than the nitrate-derived $NO_2$ is suggested to be important for soot oxidation

### 3.5. *In situ* DRIFT

The DRIFT spectra of adsorbed species on CuCe and BaCuCe10 that arise from contacting NO + $O_2$ were investigated to gain insight into the types of stored $NO_x$ species. Fig. 8 shows the IR spectra of the catalysts exposed to 1000 ppm NO + 10% $O_2$ from 50 to 450 °C. As shown in Fig. 8a, the adsorbed species are mainly chelating nitrito (1264, 1164 and 813 $cm^{-1}$), monodentate nitrito (1601–1591 and 1216–1206 $cm^{-1}$) and chelating nitro compounds (1497–1403 and 1264–1164 $cm^{-1}$) on CuCe-F at low temperatures (<200 °C) [45]. As the temperature increases, the nitrite bands are gradually replaced by those assigned to the nitrate species, including bidentate (1552–1545, 1216 and 1021 $cm^{-1}$) and monodentate nitrates (1528–1521, 1236 and 993 $cm^{-1}$) [4,33,45]. The nitrate bands are stable in the temperature range of 200–300 °C and then decline in intensity as the further increase of temperature. Considering the NO-TPO results, it is notable that the trend of $NO_2$ concentration correlates well with that of the IR intensities of nitrates versus temperature.

The formation of nitrates is delayed on the catalyst by the introduction of barium as indicated in Fig. 8b. Similarly, chelating nitrito (1264, 1157 and 814 $cm^{-1}$) and monodentate nitrito (1615 and 1209 $cm^{-1}$) are dominant on BaCuCe10-F at low temperatures. These nitrite species transform to monodentate and bidentate nitrates (1542–1528, 1296–1237 and 1032–1025 $cm^{-1}$) at 250 °C. Meanwhile, the bands ascribed to ionic $Ba(NO_3)_2$ (1768, 1396–1348 and 814 $cm^{-1}$) [25,46] begin to emerge, accompanied by minus bands due to the decomposition of $BaCO_3$ (1431, 1052 and 862 $cm^{-1}$) [25]. It means that $BaCO_3$ is gradually replaced by $Ba(NO_3)_2$ via acceptance of nitrates from the adjacent Cu $^{x+}$ and $Ce^{x+}$ active sites. $Ba(NO_3)_2$ seems to remain stable at a temperature as high as 450 °C, which enables BaCuCe10-F to store a considerable amount of $NO_x$. However, it is different in the case of NO-TPO (Fig. 7b) that the adsorbed $NO_x$ species do not seem so stable with an onset temperature of desorption below 400 °C. This difference may be related to different gas flow types applied in two experiments. The gas flow skims over the catalysts cake in in situ DRIFTS, while it goes through the catalyst bed in NO-TPO, which would make the desorption of $NO_x$ easier.

$NO_x$ storage capacity is completely lost on CuCe-HA due to severe sintering of oxides, reduced surface area and seriously weakened redox activity, as the $NO_x$-derived bands can hardly be detected during the whole temperature range measured (not shown). This does not seem to be the case with BaCuCe10-HA as two wide bands at 1528 and 1348 $cm^{-1}$ appear above 400 °C, which are ascribed to bidentate and ionic nitrates, respectively. Again, BaCuCe10-HA has a higher $NO_2$ concentration than CuCe-HA above 350 °C in NO-TPO measurement, attesting to the consistency between the IR signals of adsorbed nitrate species and the NO-TPO curve.

## 4. Discussion

Based on the experimental evidences, the mechanism of $NO_x$-assisted soot oxidation with $CuO_x$–$CeO_2$ mixed oxides is tethered to its redox activity, with $NO_2$ acting as the intermediate to transfer active oxygen from the catalyst surface onto the soot (Eqs. (1) and (2)). The mechanism differs when barium is as-loaded on $CuO_x$–$CeO_2$.The $NO_2$ does not only originate from the oxidation of gaseous NO but also from the decomposition of nitrates stored at lower temperatures (Eq. (3)), where M represents the metal active

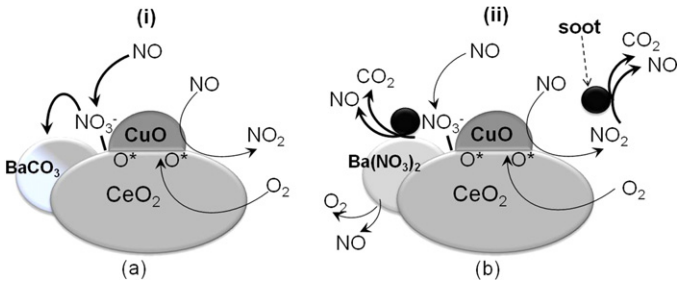


**Scheme 1.** (a) $NO_x$ storage at low temperatures and (b) $NO_x$-assisted soot oxidation on BaCuCe catalyst.

sites including $Cu^{x+}$, $Ce^{x+}$ and $Ba^{2+}$ cations. The produced $NO_2$ is then transferred onto the surface of the soot to form surface oxygen complexes (SOCs) which are further oxidized to produce $CO_x$. In addition, the surface nitrates on the catalyst may directly react with the adjacent soot particles (Eq. (4)) at the initial stage of soot oxidation. It should be noted that the NO rise does not only arise from catalytic reduction of $NO_2$ by soot but also from the thermodynamic equilibrium of the reaction $NO_2 \leftrightarrow NO + (1/2)O_2$ driven by the exothermic soot oxidation reaction:

$$M^{x+}\text{–}NO_3 \rightarrow M^{x+}\text{–}O + NO_2 \quad (3)$$

$$M^{x+}\text{–}NO_3 + C \rightarrow CO_x + M^{x+}\text{–}O + NO \quad (4)$$

Based on the analysis above as well as reports in the literature [47,48], the reaction route of catalytic soot combustion on BaCuCe can be primarily divided into three continuous steps and is summarized in Scheme 1.

(i) When the temperature is raised to 250 °C, nitrate species are preferentially formed on $Cu^{x+}$ and $Ce^{x+}$ active sites (Eq. (5)) and transferred to the adjacent barium carbonate to form barium nitrate (Eq. (6)) as shown in Scheme 1a:

$$(Cu, Ce)^{x+}\text{–}O + NO_2 \rightarrow (Cu, Ce)^{x+}\text{–}NO_3 \quad (5)$$

$$BaCO_3 + (Cu, Ce)^{x+}\text{–}NO_3 \rightarrow Ba(NO_3)_2 + (Cu, Ce)^{x+}\text{–}O + CO_2 \quad (6)$$

It should be noted that $BaCO_3$ can be transformed to $Ba(NO_3)_2$ in $NO_x$ atmosphere according to another reaction route. That is, $BaCO_3$ reacts with $NO_2$ and $O_2$ to form nitrate (Eq. (7)). The effect of metal sites (i.e. $Cu^{x+}$ and $Ce^{x+}$) lies mainly in the enhancements of NO oxidation to $NO_2$ and activation of $O_2$.

$$BaCO_3 + 2NO_2 + (1/2)O_2 \rightarrow Ba(NO_3)_2 + CO_2 \quad (7)$$

(ii) As the temperature increases to 350 °C, the stored nitrates can react with soot via the released $NO_2$ (Eq. (3)) and/or direct catalytic decomposition (Eq. (4)). As mentioned earlier, the barium nitrate is more stable compared to those coordinated to $Cu^{x+}$ and $Ce^{x+}$ sites. Thus, it seems that barium nitrate would be of less importance for soot catalytic oxidation. However, it should contribute more significantly to this reaction since the Ba-containing fresh samples show higher activities than pure $CuO_x$–$CeO_2$ mixed oxides. That is to say, the stable barium nitrate is also important for soot oxidation under a heat transfer limitation condition as shown in Scheme 1b. This is because the local heat produced from the exothermic soot oxidation reaction accelerates the decomposition of barium nitrate to the formation of NO peak at 370 °C as well as reaction between soot and barium nitrate [48].

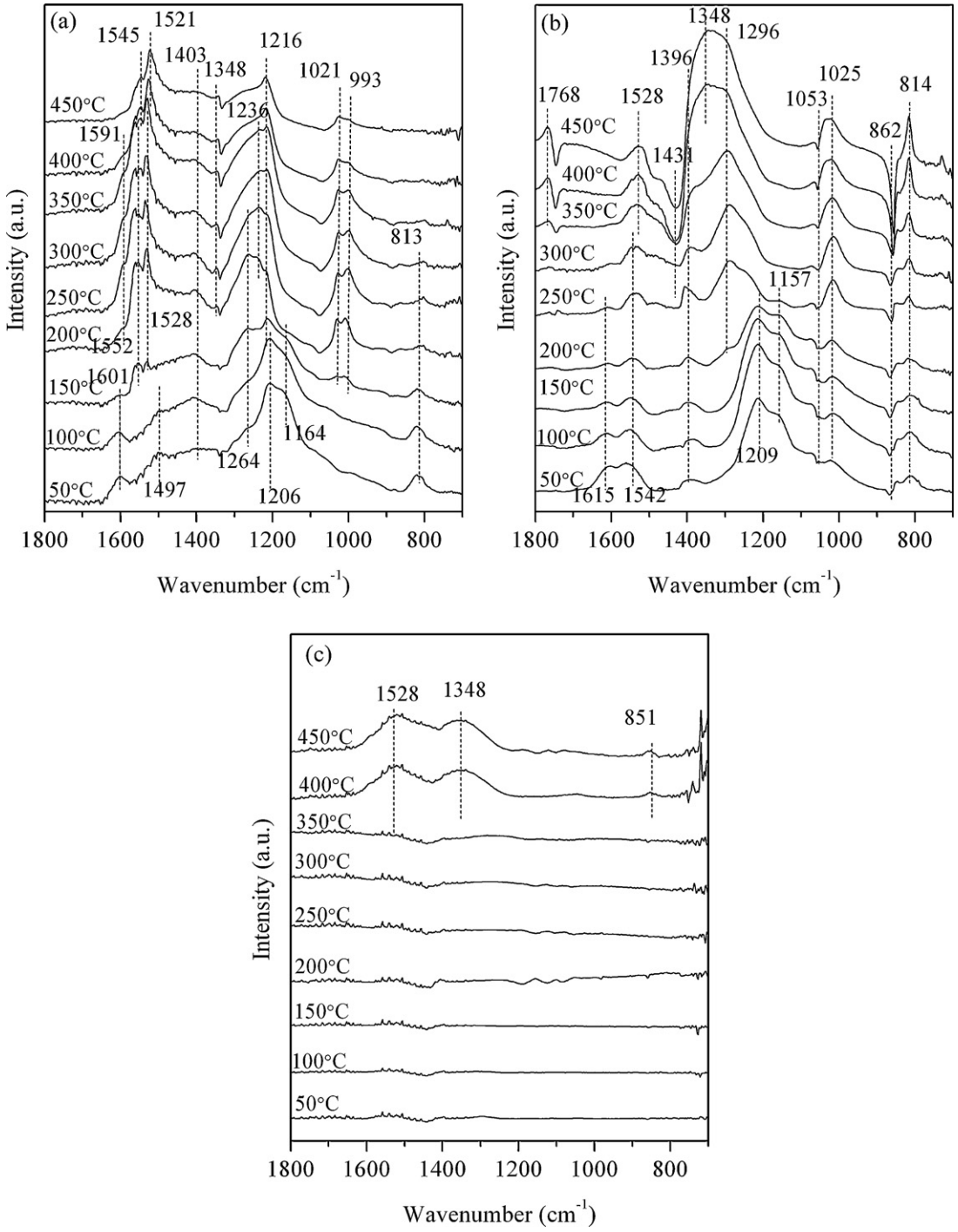


**Fig. 8.** DRIFT spectra obtained on (a) CuCe-F, (b) BaCuCe10-F and (c) BaCuCe10-HA in 1000 ppm NO/10% $O_2/N_2$ as a function of temperature.

(iii) Ultimately, the local heat initiates the extensive oxidation of soot by $O_2$ (Eq. (8)):

$$C + O_2 \rightarrow CO_2 \quad (8)$$

The hydrothermally aged BaCuCe10 experiences a dramatic loss in $NO_x$ storage capacity because of the formation of $BaCeO_3$ and the reduction of catalyst surface area. Therefore, its activity for soot oxidation depends on its ability to dominantly generate $NO_2$ via oxidation of NO, which is also weakened after aging. However, BaCuCe-HA still reveals relatively higher NO oxidation and soot oxidation activities than CuCe-HA due to the inhibition effect of barium on sintering of ceria and copper oxide crystallites, hereby maintaining stronger synergistic effect between copper oxide and ceria.

## 5. Conclusions

Ba–Cu–Ce catalysts were prepared by impregnating barium nitrate on the sol–gel-synthesized $CuO_x$–$CeO_2$ mixed oxides. The introduction of Ba onto the mixed oxides markedly enhances the soot oxidation activity of the catalyst in the presence of NO + $O_2$, especially in the low NO content atmosphere. The optimal Ba loading amount is 6–10 mol.% of the support cations (Cu + Ce), and

the obtained catalysts exhibit lower $T_i$ (376 °C) than that of CuCe (417 °C).

The $NO_x$-assisted soot combustion on BaCuCe catalysts can be divided in to three steps: (i) $NO_x$ storage, where $NO_2$ oxidized from NO is stored on the catalyst in form of nitrates when the temperature is higher than 250 °C. (ii) $NO_x$-assisted soot ignition where the nitrate- and NO-derived $NO_2$ reacts with soot above 300 °C, accompanied with a NO rise from $NO_2$ catalytic reduction and thermodynamic decomposition of $NO_2$. (iii) Extensive oxidation of soot by $O_2$, where oxygen becomes the dominant oxidant with the extensive oxidation of soot.

After hydrothermal aging at 800 °C for 10 h, BaCuCe catalysts lose the $NO_x$ storage capacity due to the formation of $BaCeO_3$ which may be avoided in the presence of $CO_2$. On the other hand, the introduction of Ba restrains the deterioration of the catalyst by inhibiting the sintering of ceria and copper oxide crystallites. The redox property of $CuO_x$–$CeO_2$ based catalysts depends on the synergistic effect between copper oxide and ceria, which is in turn determined by the crystallite size of ceria and dispersion of copper oxide to a large degree. Therefore, BaCuCe maintains a higher activity for NO oxidation than CuCe after aging. The NO-derived $NO_2$ acts as the dominant oxidant for assisting the catalytic oxidation of soot with the aged catalyst instead of the nitrate-derived $NO_2$.

## Acknowledgements

The authors would like to acknowledge Projects 2010CB732304 supported by the Ministry of Science and Technology of China and 51072096 supported by NSFC.

## References

[1] A. Setiabudi, M. Makkee, J.A. Moulijn, Appl. Catal. B 50 (2004) 185.
[2] B.A.A.L. van Setten, M. Makkee, J.A. Moulijn, Catal. Rev. 43 (4) (2001) 537.
[3] M. Jeguirim, V. Tschamber, P. Ehrburger, Appl. Catal. B 76 (2007) 235.
[4] A. Setiabudi, J. Chen, G. Mul, M. Makkee, J.A. Moulijn, Appl. Catal. B 51 (2004) 9.
[5] K. Shimizu, H. Kawachi, A. Satsuma, Appl. Catal. B 96 (2010) 169–175.
[6] I. Atribak, A.B. López, A.G. García, J. Catal. 259 (2008) 123.
[7] F.E.L. Suárez, A.B. López, M.J.I. Gómez, Appl. Catal. B 84 (2008) 651.
[8] D. Reichert, H. Bockhorn, S. Kureti, Appl. Catal. B 80 (2008) 248.
[9] Q. Liang, X. Wu, D. Weng, Z. Lu, Catal. Commun. 9 (2008) 202.
[10] J. Liu, Z. Zhao, J. Wang, C. Xu, A. Duan, G. Jiang, Q. Yang, Appl. Catal. B 84 (2008) 185.
[11] Z. Zhang, D. Han, S. Wei, Y. Zhang, J. Catal. 276 (2010) 16.
[12] V.S. Escribano, E.F. López, J.M. Gallardo-Amores, C. Del, H. Martínez, C. Pistarino, M. Panizza, C. Resini, G. Busca, Combust. Flame 153 (2008) 97.
[13] H. Muroyama, S. Hano, T. Matsui, K. Eguchi, Catal. Today 153 (2010) 133–135.
[14] J. Xu, J. Liu, Z. Zhao, J. Zheng, G. Zhang, A. Duan, G. Jiang, Catal. Today 153 (2010) 136–142.
[15] H. Shimokawa, H. Kusaba, H. Einaga, Y. Teraoka, Catal. Today 139 (2008) 8–14.
[16] V.G. Milt, M.L. Pissarello, E.E. Miró, C.A. Querini, Appl. Catal. B 41 (2003) 397.
[17] J. Liu, Z. Zhao, C. Xu, A. Duan, L. Zhu, X. Wang, Appl. Catal. B 61 (2005) 36.
[18] H. An, P.J. McGinn, Appl. Catal. B 62 (2006) 46.
[19] D. Weng, J. Li, X. Wu, F. Lin, Catal. Commun. 9 (2008) 1898.
[20] E. Aneggi, C. Leitenburg, G. Dolcetti, A. Trovarelli, Catal. Today 136 (2008) 3.
[21] P. Broqvist, H. Grönbeck, E. Fridell, I. Panas, Catal. Today 96 (2004) 71.
[22] J.M. Coronado, J.A. Anderson, J. Mol. Catal. A 138 (1999) 83.
[23] B. Westerberg, E. Fridell, J. Mol. Catal. A 165 (2001) 249.
[24] Y. Su, M.D. Amiridis, Catal. Today 96 (2004) 31.
[25] V.G. Milt, C.A. Querini, E.E. Miró, M.A. Ulla, J. Catal. 220 (2003) 424.
[26] M.A. Peralta, V.G. Milt, L.M. Cornaglia, C.A. Querini, J. Catal. 220 (2003) 424.
[27] V.G. Milt, E.D. Banús, M.A. Ulla, E.E. Miró, Catal. Today 133–135 (2008) 435.
[28] L. Sui, L. Yu, Chem. Eng. J. 142 (2008) 327.
[29] K. Krishna, M. Makkee, Catal. Today 114 (2006) 48.
[30] L. Castoldi, R. Matarrese, L. Lietti, P. Forzatti, Appl. Catal. B 64 (2006) 25.
[31] X. Wu, S. Liu, F. Lin, D. Weng, J. Hazard. Mater. 181 (2010) 722.
[32] X. Wu, Z. Zhou, D. Weng, F. Lin, Catal. Commun. 11 (2010) 749.
[33] X. Wu, Q. Liang, D. Weng, Z. Lu, Catal. Commun. 8 (2007) 2110.
[34] X. Wu, F. Lin, D. Weng, J. Li, Catal. Commun. 9 (2008) 2428.
[35] J. Chen, Y. Zhan, J. Zhu, C. Chen, X. Lin, Q. Zheng, Appl. Catal. A 377 (2010) 121.
[36] W. Shan, W. Shen, C. Li, Chem. Mater. 15 (2003) 4761.
[37] Y. She, Q. Zheng, L. Li, Y. Zhan, C. Chen, Y. Zheng, X. Lin, Int. J. Hydrogen Energy 34 (2009) 8929.
[38] B.R. Stanmore, V. Tschamber, J.-F. Brilhac, Fuel 87 (2008) 131.
[39] R. Strobel, F. Krumeich, S.E. Pratsinis, A. Baiker, J. Catal. 243 (2006) 237.
[40] M. Yan, Y. Li, J. Wang, M. Shen, J. Catal. 271 (2010) 228–238.
[41] M. Casapu, J.D. Grunwaldt, M. Maciejewski, M. Wittrock, U. Göbel, A. Baiker, Appl. Catal. B 63 (2006) 232.
[42] H. Chen, H. Zhu, Y. Wu, F. Gao, L. Dong, J. Zhu, J. Mol. Catal. A 255 (2006) 254.
[43] P. Zimmer, A. Tschöpe, R. Birringer, J. Catal. 205 (2002) 339.
[44] F. Giordano, A. Trovarelli, C.D. Leitenburg, M. Giona, J. Catal. 193 (2000) 273.
[45] K.I. Hadjiivanov, Catal. Rev. Sci. Eng. 42 (2000) 71.
[46] V.G. Milt, M.A. Ulla, E.E. Miró, Appl. Catal. B 57 (2005) 17.
[47] A.L. Kustov, M. Makkee, Appl. Catal. B 88 (2009) 263.
[48] L. Castoldi, N. Artioli, R. Matarrese, L. Lietti, P. Forzatti, Catal. Today 157 (2010) 384.